Effect of the deposition route on the microstructure of plasma-sprayed hydroxyapatite coatings

Marine Chambard, Olivier Marsan, Cédric Charvillat, David Grossin, P. Fort, Christian Rey, François Gitzhofer, Ghislaine Bertrand

Effect of the deposition route on the microstructure of plasma-sprayed hydroxyapatite coatings

Marine Chambard[a,b,*], O. Marsan[a], C. Charvillat[a], D. Grossin[a], P. Fort[c], C. Rey[a], F. Gitzhofer[b], G. Bertrand[a]

[a] CIRIMAT, Université de Toulouse, CNRS, INP-ENSIACET 4 allée Emile Monso, BP44362, 31030 Toulouse cedex 4, France
[b] CREPE, Dept. of Chemical and Biotechnological Engineering, Université de Sherbrooke, Sherbrooke, QC, Canada
[c] PROJECTION PLASMA SYSTEME (2PS), 4 du Colombier, 12220 Montbazens, France

ARTICLE INFO

Keywords:
Rf - suspension plasma spraying
APS
Hydroxyapatite coating
Microstructure
Precursor nature

ABSTRACT

Plasma-spray (PS) is the most common technique used to cover orthopaedic titanium-based implant surfaces with hydroxyapatite (HA - $Ca_{10}(PO_4)_6OH_2$). The objective of the current work was to explore the influence of the precursor nature and characteristics (mainly powder size, Ca/P ratio, and density) on the morphology and the microstructure of HA coatings, deposited either by conventional atmospheric plasma spray (APS) or by rf-suspension plasma spray (rf-SPS). Two powders with different size distribution, density and shape were sprayed with same operating APS conditions. In parallel two water-based suspensions with distinct particle size and chemistry (Ca/P ratio) were implemented in rf-SPS. The morphology of both APS and rf-SPS coatings observed by SEM exhibits micro and sub-micro sized structures respectively, with similar porosity and thickness. The difference in precursor particle size does not affect the coating structure in rf-SPS, unlike in APS conditions. Superimposition of topography and phases maps performed from profilometry and Raman cartographies showed no direct correlation between the surface profile and composition. But such analysis highlighted the heterogeneity of the phases composing the coating surface, opening the possibility of a better understanding of biological behaviour.

1. Introduction

Every year in Canada and in France, around 4 to 5% more hip and knee joints are implanted for medical (traumas, diseases such as obesity) and demographic (aging of the population) reasons [1]. An increasing number of these prostheses are currently made of a bioinert metal coated with hydroxyapatite (HA), whose crystalline structure and chemical composition are very close to those of the mineral part of bones. This calcium phosphate ($Ca_{10}(PO_4)_6OH_2$) is the preferred material in the field of orthopedics for its osteoconductive and biocompatible properties [2–5]. Hence, hydroxyapatite coatings on titanium-based implants (Ti-4Al-6V) have been used since the mid-1980s for their ability to promote early osteointegration and subsequent stability without the help of a cement. Various processes were investigated to produce those calcium phosphate (CaP) coatings, but national agencies (FDA, ANSM...) only approve the plasma spray techniques, for their ability to produce coatings with targeted thickness and appropriate mechanical and biological properties [6,7]. More specifically, APS (Atmospheric Plasma Spraying) is the conventional technique favored by industrials, for its moderate cost, ease of implementation and high production rate.

Nevertheless, plasma-sprayed coatings can be partly resorbed after implantation, mainly because of the presence of small amounts of calcium phosphate phases (tetracalcium phosphate TTCP, tricalcium phosphate TCP, oxyapatite OA, amorphous calcium phosphate ACP, calcium oxide CaO), more soluble than hydroxyapatite in biological medium [8,9]. These minor unintended phases result from the decomposition of HA during spraying, caused by the very high temperatures encountered into the plasma jet and subsequent quenching ($\approx 10^4$–10^6 K·s^{-1}) of the molten particles onto the cooled substrate. The following reactions describe the decomposition of HA depending on temperature.

Successive dehydroxylation of hydroxyapatite into oxyhydroxyapatite (OHA) and oxyapatite depending on vapor pressure:

$$Ca_{10}(PO_4)_6(OH)_2 \underset{850°C}{\leftrightarrow} Ca_{10}(PO_4)_6O_x(OH)_{2-2x} + x\,H_2O \quad (1a)$$

$$Ca_{10}(PO_4)_6O_x(OH)_{2-2x} \underset{1050-1500°C}{\leftrightarrow} Ca_{10}(PO_4)_6O + (1-x)\,H_2O \quad (1b)$$

* Corresponding author at: 4 allée Emile Monso, 31030 Toulouse, France.
E-mail address: marine.chambard@ensiacet.fr (M. Chambard).

https://doi.org/10.1016/j.surfcoat.2019.01.027

$$Ca_{10}(PO_4)_6O \xleftrightarrow[1360\text{-}1570\ ^\circ C]{} Ca_4(PO_4)_2O + 2\ Ca_3(PO_4)_2$$

OA TTCP α̅/β-TCP (2)

$$Ca_4(PO_4)_2O \xleftrightarrow[1700^\circ C]{} CaO + 2\ Ca_3(PO_4)_2$$

TTCP α̅/β-TCP (3)

$$Ca_3(PO_4)_2 + Ca_4(PO_4)_2O \underset{1750^\circ C}{\leftrightarrow} CaO + \text{liquid phase.} \quad (4)$$

As suggested by Overgaard [10], coating loss might not be intrinsically a problem if enough coating is replaced by bone to sustainably fix the implant, although one may question the metal-bone interface quality. This addresses the importance of the coating quality (purity, crystallinity, microstructure, porosity, roughness, thickness, mechanical properties…) [11].

Depending on the spraying conditions (nature of the plasma gases, presence of water etc.), various degrees of decomposition occur. The presence of these phases at the substrate coating interface or into the coating gradually weakens it by a dissolution process until its possible failure and scaling [4,12–14]. There is thus an increasing need for hip prosthesis with a better mechanical stability for the long term, in order to reduce health care costs and traumas caused by revisions which represented > 8% of all the prostheses implanted in 2014–2015 in Canada [1]. An accurate quantification and localization of the decomposed phases which are present in plasma sprayed coatings is thus essential.

Besides, research recently enlightened the interest of producing nanostructured coatings to bring their structure closer to that of the natural bone. Such a coating is of biological and mechanical interest since Webster et al. [15] have demonstrated that osteoblastic activity on bulk hydroxyapatite synthesized by precipitation and sintered at 1100 °C is enhanced by decreasing the grain sizes from a micro to a nanometric range [16], the transition value being established around 100 nm. This strategy was also applied to the coatings production and has demonstrated tensile strength adhesion values in accordance with standards (15 MPa for adhesion test in ISO 13779-2:2008) and good cell attachment and proliferation behaviours. The elaboration of these nanostructured coatings has been achieved by using a suspension (liquid feedstock containing submicronic to nanometric solid particles) instead of a powder to be injected in the plasma spray system (SPS) [17–19]. The Université de Sherbrooke invented the rf-suspension plasma spray in the 1990s, and since then has worked on materials and systems developments using this technology. The supplementary advantages of a liquid feedstock rely on a larger tuning of the chemistry of the precursors and distinct composition and temperature of the plasma. Such characteristics are expected to enable a better control of the coatings composition, and possibly limiting the decomposition of the hydroxyapatite under optimised conditions [20]. Indeed, the solvent makes the plasma cooler but can enhance the particle treatment. The introduction of more species to be ionized increases on one hand the thermal conductivity of the plasma mixture (and thus the heat flux perceived by the particles), and on the other hand cools it down by consuming the power of the torch [21,22]. Not to mention the fact that the presence of water vapor shifts the balance in favor of the conservation of hydroxyapatite according to *Le* Châtelier's principle in eqs. (1a) and (1b).

It has also been shown that certain characteristics, such as surface roughness and porosity, influence the bioactivity of the hydroxyapatite coating in the short and long term, since they define the surface area that interacts with the different proteins [23,24]. It has been largely demonstrated that the higher the roughness the better the osseointegration of the coating [25,26]. Crystallinity is also a critical parameter in the cell behaviour as mentioned in the review of Surmenev et al. [27]. A highly crystallized coating has been proven to increase the cell proliferation and adhesion compared to a poorly crystallized coating for identical particle size. Moreover, nanosized crystallites favored good cell attachment and spreading compared with uncoated Ti [16].

The present study aims at determining the impact of the particles characteristics (density, Ca/P ratio and size distribution) used in the suspension on the roughness, microstructure, and composition of the coatings obtained by rf-SPS. To better assess the rf-SPS coatings microstructure, a comparison is performed with coatings synthesized by conventional APS implementing optimised commercial conditions with two different powders.

2. Experimental methods

2.1. Material

2.1.1. Substrates

Titanium alloy Ti-6Al-4V (grade 5) was selected as the substrate material for its sufficient mechanical strength, anti-corrosion and bioinert properties [4,28].

For both rf-SPS and APS processes, prior to plasma spraying, plates of 75 × 55 × 1.6 mm^3 were cleaned with solvents (ethanol and acetone in ultrasonic bath) and grit-blasted with alumina (F46) at an incidence angle of 90°, a 120 mm blasting distance and a pressure of 4.5 bar. The arithmetic roughness of the surface (Sa) was determined with a profilometer to be approximately 4 µm.

2.1.2. Rf-SPS powders

Two powders (K-SPS and Q-SPS) were synthesized to produce the suspensions for rf-SPS plasma spraying. Calcium nitrate tetrahydrate ($Ca(NO_3)_2$, $4H_2O$ – Sigma Aldrich), diammonium phosphate ($(NH_4)_2HPO_4$ - Fischer) and NH_4OH solution at 20 wt% (Fischer) were used as chemical precursors for Ca^{2+}, PO_4^{2-} and OH^-. The calcium phosphates were obtained by coprecipitation according to the following balanced chemical equation:

$$10\ Ca(NO_3)_2 + 6\ (NH_4)_2HPO_4 + 8\ NH_4OH \rightarrow Ca_{10}(PO_4)_6OH_2 + 6\ H_2O + 20\ NH_4NO_3. \quad (5)$$

The powder synthesis protocols were adapted from protocols described by Kannan [29] and Al-Qasas [30], respectively for K-SPS and Q-SPS. The main differences between the K-SPS and Q-SPS adapted protocols rely on the reactants feed rates and concentrations, as well as the maturation time. The pH is maintained at 9 all along the reaction by adding 20 wt% NH_4OH to obtain the appropriate acidity of the phosphate ion leading to an apatitic structure. The Ca/P ratio of the precursors is set to 1.67 to promote the formation of stoichiometric hydroxyapatite. After the maturation time, the powders are filtered and washed with 10 times the reaction medium volume of water before freeze-drying (pressure of 0.10 mbar, −80 °C for 3 days).

2.1.3. APS powders

Two types of hydroxyapatite powders were used: a sintered one purchased from Teknimed (Blocky, density of 0.87 g/cm^3, D_{50} of 167 µm) and a spray-dried one from Medicoat (SD, density of 0.54 g/cm^3, D_{50} of 97 µm). Both powders are fully crystallized and pure hydroxyapatite (> 98 vol%) as determined by X-ray diffractometry before and after calcination at 1000 °C for 15 h.

2.2. Plasma spraying parameters

The operating conditions of both techniques are reported in Table I. APS coatings were produced under optimised commercial conditions by 2PS in Montbazens with a GT5 2PS torch, under reducing conditions (Ar/H_2). Rf-SPS coatings were produced at the Université de Sherbrooke (Québec) with plasma generated by a 50-kW RF plasma torch operating at 3 MHz (PL-50 model from Tekna Plasma System Inc.). The suspension was injected by a

Table I
Plasma spraying parameters used for APS and rf-SPS[a].

Technique	APS	rf-SPS
Power (kW)	30	35
Plasma gas	Ar/H_2 (plasma) and Ar (carrier)	Ar (23 slpm)
Carrier Gas	(70–75 slpm in total)	Ar (12 slpm)
Sheath Gas	n.a.	Ar/O_2 (12/50 slpm)
Pressure (torr)	750	100
Working distance (mm)	App. 100	200
Solid content of the suspension (wt%)	n.a.	13

[a] To preserve and ensure their expertise as manufacturer, 2PS keeps confidential some elements related to APS technique.

peristaltic pump at a feeding rate of 10 mL/min with a solid load of 13 wt%. The liquid atomisation probe was designed by Tekna, with an output diameter of 0.8 mm. The composition of the plasma is a mixture of Ar and O_2, based on previous work performed by Loszach et al. [17] that pointed out the excess of HA decomposition caused by the use of H_2 due to its very high thermal conductivity (3.74 $W{\cdot}m^{-1}{\cdot}K^{-1}$) and diatomic nature, increasing the plasma density. But argon is a monoatomic gas with low thermal conductivity (0.64 $W{\cdot}m^{-1}{\cdot}K^{-1}$) and it is not energetic enough if used alone. Oxygen is therefore the most appropriate secondary gas (1.37 $W{\cdot}m^{-1}{\cdot}K^{-1}$) in this case.

2.3. Characterization of powders and coatings

All the following characterizations were performed in line with ISO standard 13,779–2:2008 and 13,779-3:2008 [31,32].

2.3.1. Particle size distribution

The particle size distribution was measured with a Malvern Mastersizer Hydro 2000S granulometer (UK) in aqueous media, with ultrasound for SPS and Blocky-APS powders. Ultrasound was not used in the case of the SD-APS powder because it caused the particles to break down into smaller pieces, distorting the results. The measuring cell reservoir was kept under agitation at 1750 rpm for all trials.

2.3.2. Ca/P ratio of powders

The chemical composition of the powders was established by complexometric titration with EDTA for the determination of the calcium content and UV spectrophotometry determination of the phosphovanadomolybdic complex for the phosphorus content. It was then confirmed by XRD analysis on calcined powders, according to the procedure provided by the standard ISO 13779-3 implying the use of standards of known composition.

2.3.3. Topography

The roughness of the substrates and the deposited coatings was evaluated using a Sensofar S-Neox confocal microscope (Barcelona, Spain) at ×10 magnification. The average value was determined from 5 scanning zones of 1750 × 1300 µm at 0, 90°, 180° and 270°.

2.3.4. Crystalline phases

The phase analysis of the powders was investigated using D8 diffractometer (Bruker AXS GmbH, Karlsruhe, Germany) with Cu Kα radiation (λ = 1.5406 Å) produced at 40 kV and 50 mA. Data were recorded in the 20°–60° 2θ range with a step size of 0.02° and 38 s per step. The patterns were identified using Match! Software and Rietveld refinements were realized using Maud software [33] with a fixed background, based on the following JCPDS data:

- HA, hydroxyapatite, JCPDS no. 00-009-0432;
- α-TCP, tricalcium phosphate $Ca_3(PO_4)_2$, JCPDS no. 04-018-9895;
- β-TCP, tricalcium phosphate $Ca_3(PO_4)_2$, JCPDS no. 00-070-2065;
- TTCP, tetracalcium phosphate, $Ca_4P_2O_9$, JCPDS no. 00-025-1137;
- CaO, calcium oxide, JCPDS no. 04–011-9020.

Amorphous phase was considered during Rietveld refinement but only for purposes of comparison between coatings, since this method is not accurate enough [34].

The crystallinity ratio R_1 was calculated according to the formula proposed in the standard ISO 13779-3, involving the use of a fully crystallized standard (hydroxyapatite calcined at 1000 °C for 15 h):

$$R_1 = \frac{\textit{Integrated intensity of 10 lines of the sample}}{\textit{Integrated intensity of 10 lines of the standard}} \times 100. \quad (6)$$

Crystallite sizes d were estimated by Scherrer approximation:

$$d = K\lambda / h_{1/2} \cos\theta \quad (7)$$

where K is the broadening constant varying with the crystal shape and chosen to be 0.9 to fit with the elongated shape of crystalline apatite, θ the scattering angle, λ the wavelength of the incident radiation (Cu Kα = 1.5418740 Å), $h_{1/2}$ the value of full width at half-maximum intensity of the peaks of the (002) and (300) planes, representative of the crystallites along c- and a-axes respectively. The size of crystallites is roughly estimated with this equation because of the imprecision of certain parameters such as K and the fact that the peaks of interest are out of the range 2θ = 30°–50°, which generates peak asymmetry and compromise profile analysis.

2.3.5. Non-crystalline phases

Fourier Transform Infrared FTIR analysis was carried out on powders with a PerkinElmer 1700 spectrometer (USA) at a resolution of 4 cm^{-1} and KBr pellets, in the 400–4000 cm^{-1} range.

Raman spectra of the coating were recorded with a Labram HR 800 confocal microscope (Horiba Jobin-Yvon, Japan) equipped with a λ = 532 nm radiation, in the 100–4000 Raman shift range. A semi-quantitative evaluation of the different bands constituting the ν_1PO_4 domain was performed using Labspec 5 curve-fitting software, based on the peak positions given by Rey et al. [35]. This analysis is useful to evaluate the presence of phases like the amorphous calcium phosphate (ACP) and the oxyapatite (OA), two phases difficult to identify by XRD.

To characterize the surface and cross section phase homogeneity of the coatings, the integrated intensity of the ν_1 PO_4 hydroxyapatite peak I^{HA} was measured on a 290 × 440 and 70 × 55 $µm^2$ area for the surface and cross section respectively, as well as the sum of the integrated intensity of the ν_1 PO_4 lines of all the other undesirable calcium phosphate phases (OP) mentioned before. A spot size of 5 $µm^2$ was used and

Table II
Raman line positions composing v_1 band in plasma-sprayed calcium phosphate coatings [35].

Phase	Characteristic peaks in v_1 band
Hydroxyapatite HA	964 vs
Tricalcium phosphate α-TCP	976 s, 964 s, 954 sh
Tricalcium phosphate β-TCP	970 s, 948 s
Tetracalcium phosphate TTCP	983 vw, 961 vs, 956 vs, 946 s, 940 s
Amorphous calcium phosphate	950 s
Oxyapatite	951 s, 966 s

spectra were collected in the 900–1000 shift range for the surface, and a spot size of 1.2 μm^2 in the case of the cross section. As a lot of phases are possibly present (HA, TTCP, TCP, ACP and OA, Table II), it can be hard to distinguish and dissociate all the bands included in this domain. But since hydroxyapatite is present in much higher proportion, it is easy to isolate it from the others. By calculating the ratio R_2 (Eq. (8)), it is possible to localize HA-rich areas and HA-poor areas.

$$R_2 = I^{HA}/(I^{HA} + I^{OP}) \quad (8)$$

with $I^{OP} = I^{TTCP} + I^{\alpha-TCP} + I^{\beta-TCP} + I^{ACP} + I^{OA}$.

2.3.6. Morphology

APS and rf-SPS powders and coatings were observed by SEM with a LEO 435 VP (Semtech, USA), using the back-scattering mode at 15 kV, 1.6 nA probe current and 12 mm working distance. To determine the porosity from the cross-section, the samples were cut, then mounted and vacuum impregnated with cold epoxy. They were then ground and polished in accordance with the procedure described by Geels et al. [36]. Image analysis was performed with ImageJ on 10 different pictures, by manual thresholding and despeckling.

3. Results and discussion

3.1. Characteristics of powders

3.1.1. Particle size and morphology

The size distributions of all powders are monomodal curves, centered around 100–150 μm for APS powders and 3–9 μm for synthesized K and Q-SPS powders. The span parameter calculated between the 10% and 90% points and normalized to the mid-value ($D90 - D10)/D50$ evidences the width of the size distribution (Table III). K and Q-SPS powders display a similar but twofold higher span parameter, indicating a wider size distribution compared with APS powders, whose span parameters are equal to 1.

Both SPS powders have similar shapes with irregular granular faces and edges. The K particles are visibly larger than the Q particles but do not show an acicular shape, contrary to what is usually observed for apatite particles. APS powders morphologies are quite different: as expected, the Blocky-APS particles display an angular shape whereas the SD-APS ones are more spherical [30].

3.1.2. Structural analysis

The Ca/P ratio of Q-SPS synthesized powders and of both commercial powders is around 1.67, close to the ratio of a stoichiometric HA whereas for the K-SPS synthesized particles, it is around 1.62 as reported in Table III.

XRD patterns of all powders (Fig. 1) show the typical crystallographic apatitic structure of $Ca_{10}(PO_4)_6(OH)_2$ (JCPDS 00–009-432), where no secondary phase is detected. Poorly crystallized apatite is identified in the case of K-SPS, represented by a broad and barely visible peak centered around $2\theta = 30.5°$ [37,38]. The crystallite sizes are large and similar for both APS powders (about 200 nm along the a-axis) while they are quite small in the case of the Q-SPS and even more for the K-SPS powders (75 and 20 nm along the a-axis respectively). This is probably the consequence of the high reactant feed rate implemented in the K-SPS synthesis compared with the Q-SPS, which favored nucleation over crystal growth.

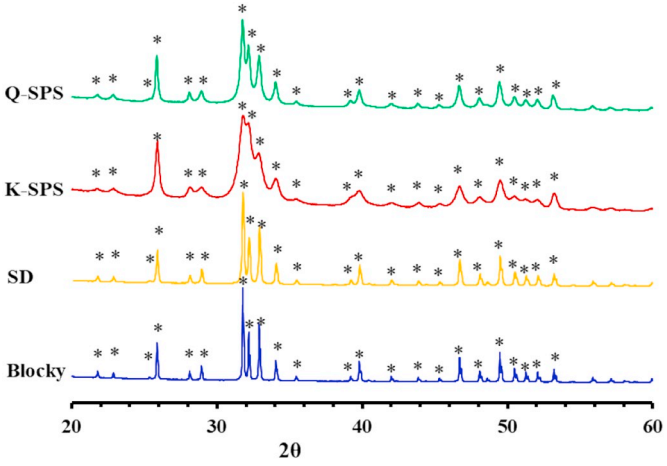

Fig. 1. XRD of powders: K-SPS, Q-SPS, Spray-dried SD and Blocky.

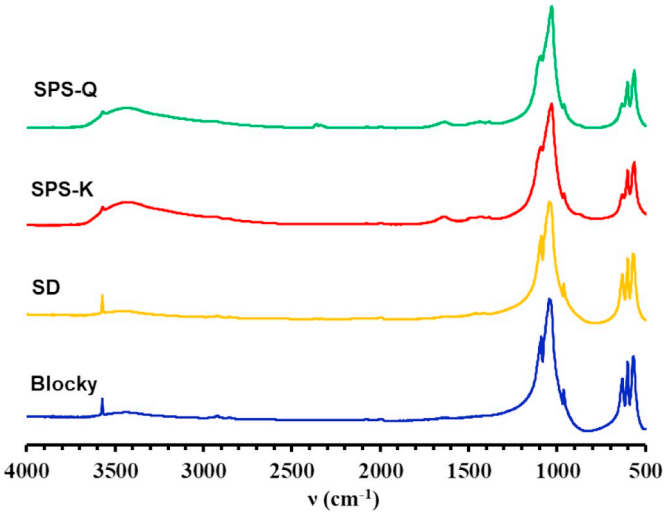

Fig. 2. FTIR spectra of K-SPS, Q-SPS, SD and Blocky powders.

FTIR spectra of commercial and synthesized powders are presented in Fig. 2 and are typical of an hydroxyapatite [39,40]. As expected, APS commercial powders spectra exhibit strong peaks at 632 ± 1 and 3570 ± 2 cm^{-1}, attributed respectively to the libration mode of the hydroxyl group OH^- and to its stretching mode ν_s, characteristic of the hydroxyapatite phase. In contrast, these peaks are weak in the case of K-SPS and Q-SPS, which might indicate that the apatite is not fully hydroxylated. Additional weak lines at 1400–1500 cm^{-1} in these last samples indicate the presence of carbonate ions, confirmed by the presence of a shoulder at 872 cm^{-1}. This last line could also point out the existence of a few HPO_4^{2-} groups in these CaP structures, typical for calcium deficient hydroxyapatite ($Ca/P < 1.667$), as mentioned by Raynaud et al. [41]. The broad peak around 3430 ± 20 cm^{-1} and Q-SPS powders reveals a significant amount of water most probably adsorbed to the surface of these nanosized crystalline powders. Indeed, it is relevant to consider that during the freeze-drying step not all water

Table III
Main characteristics of rf-SPS and APS precursors.

Powder	Ca/P ratio	D10 (μm)	D50 (μm)	D90 (μm)	$\frac{D90-D10}{D50}$	Crystallinity ratio (%)	Crystallite size for (002) plan (nm)	Crystallite size for (300) plan (nm)
K-SPS	1.62 ± 0.02	2.8 ± 0.1	9.3 ± 0.9	24 ± 3	2.3	70	176	20
Q-SPS	1.66 ± 0.01	1.5 ± 0.02	3.0 ± 0.1	7.6 ± 0.9	2.0	72	n.d.	75
Blocky	1.667	104 ± 1.7	167 ± 3	267 ± 7	1.0	95	255	185
SD	1.667	57.2 ± 3.1	96.8 ± 1.4	154 ± 4	1.0	107	281	208

Table IV
Coatings main characteristics.

	APS		rf-SPS	
Powder used	Blocky	SD	K-SPS	Q-SPS
Rietveld refinement	Similar coatings with 90% of HA and few phases other than HA		Less HA than APS, more TTCP in Q-SPS and more TCP in K-SPS coatings	
Porosity (%)	15.8 ± 2.4	19.4 ± 3.1	14.4 ± 3.0	19.3 ± 4.2
Thickness (µm)	137 ± 15	112 ± 20	78 ± 12	46 ± 21
Roughness				
Sa (µm)	11.9 ± 0.6	12.5 ± 0.4	6.3 ± 0.8	6.3 ± 0.2
Sz (µm)	122 ± 18	127 ± 15	125 ± 45	176 ± 28
Ssk	≈0.1	≈−0.1	≈0.8	≈0.9

molecules evaporate from the surface of the powder.

The powders for APS have the same crystalline structure (well-crystallized hydroxyapatite) and size (200 nm) but different powder shapes and size distributions. Q and K-SPS powders have similar poorly crystallized non-stoichiometric apatitic structure with nanosized crystals but different powder size distributions.

3.2. Rf-SPS and APS coatings

3.2.1. Top-surface analysis

3.2.1.1. Topography. The average area roughness Sa of APS and rf-SPS coatings was evaluated to be around 12 µm and 6 µm respectively as reported in Table IV. As expected, APS coatings are rougher than rf-SPS coatings due to the large feedstock particles implemented, even though the substrate roughness was equivalent for both techniques. High roughness is usually related to high exposed surface which gives more sites for the proteins and molecules to anchor [23], making the present APS coatings more suitable from this point of view. The Sz and Ssk parameters are similar for both APS-coatings. Even if the particle size and shape of blocky and SD powders can possibly affect the coating topographical characteristics, it was not the case in this study because of the spraying conditions which have been developed by the company to produce very similar coatings. For rf-SPS coatings, the Sz parameter value is 40% higher with Q suspension compared with K suspension but the skewness Ssk parameter values are alike. The topography of both rf-SPS coatings is therefore very similar except for the Sz value which is sensitive to the relative size of particles vs substrate roughness. Indeed, Q-SPS particles have a diameter 3 times smaller than K-SPS particles and therefore can emphasize substrate topographic defaults and consequently exhibit higher peak-valley (Sz) value. For all coatings (APS or rf-SPS) the Ssk value is either equal to zero or very low which means that the surface topography is homogeneous without distortions like a plateau with peaks or valleys.

SEM images of APS coatings reported on Fig. 3a and b show large microstructures, heterogeneous surfaces made of a mixture of fully and partially melted areas with very few cracks compared with rf-SPS coatings, implying that the spraying conditions are better controlled from a thermal point of view. Independently from the feedstock characteristics, SD and blocky-powder, the morphology of the APS coating surfaces is very similar. In the case of powder plasma spraying, the mean splats diameters are typically 2 to 6 times [18] larger than the diameter of the CaP droplet before impact. Since the splats are hardly visible and measurable for both coatings, such a correlation with the feedstock particle sizes is complex. On Fig. 3 c and d, the surfaces of K-SPS and Q-SPS coatings do not show any significant difference. Microcracks are visible on both surfaces, which should be avoided with better control of the preheating temperature of the substrate, to reduce the thermal expansion gradient between the coating and the substrate [4,42]. Fully molten lamellae are clearly evidenced with sintered-porous zones in between, which contain micrometric to submicrometric particles. Splat diameters are very similar for rf-SPS coatings (averaging 8–9 µm on the upper surface), which means that particles size implemented in K-SPS and Q-SPS centered at 3 or 9 µm respectively does not have a significant impact on the surface morphology, as already evidenced by the roughness study. In rf-SPS, it is the CaP droplet size before impact that determines the splat diameters. Conceding that the splat flattening ratio mentioned above for conventional plasma spraying is applicable to rf-SPS, the splat diameters ranging from about 3 to 25 µm could originate from CaP droplets ranging from 0.5 to 12 µm in diameter before impact. These CaP droplets are produced from the suspension atomized drops whose size depends on the suspension (viscosity, suspension density, atomization mode) and the plasma characteristics. Assuming that both suspensions have similar viscosities and undergo an atomization comparable to that of water, drops of approximately 50 µm in diameter should be formed at the output of the probe. For an atomized drop with a 13 wt% solid load (4.3 vol% for stoichiometric hydroxyapatite powder with a density of 3.15 kg/m^3), the final CaP droplets should have a diameter of about 17 µm, which is in the expected range. Fragmentation is expected to be low, as stated in the literature due to the typical slow plasma jet velocity of rf-SPS technique (< 500 m/s) [43]. But calculating the Weber number *We*, which is the ratio of the impact energy to surface energy (Eq. (9)), with d_1 the droplet diameter, u_r the gas-liquid relative velocity, ρ_g the gas density and σ_1 the liquid surface tension, it seems to exceed the limit value below which fragmentation is absent ($We = 14$) [18]:

$$We = \rho_g u_r^2 d_1/\sigma_1. \quad (9)$$

If fragmentation occurs and takes place prior to the CaP particle melting, it may be easier for Q-SPS atomized drops than for K-SPS drops, due to the smaller size of the precursor particles in the case of Q powder. Droplets coming from Q-SPS fragmentation are thus likely to be smaller than their counterpart K-SPS droplets, which confers them a lower kinetic energy and less chances of impacting the substrate. This could explain why K-SPS coating is about 80 µm thick while Q-SPS coating is about 50 µm and why both coatings have similar splat diameters.

3.2.1.2. Phases composition. X-ray diffraction data of the surfaces (Fig. 4) were analysed by Rietveld refinement which allowed the identification and semi-quantification of the crystalline phases (Table IV). The crystallinity ratio is beyond 45% in all coatings and in accordance with the standards. Apatite is detected as being the major crystalline phase, but some other calcium phosphates are identified such as TCP, TTCP, ACP and CaO. Their presence indicates that hydroxyapatite underwent sufficient temperature, thermal exchanges or residence time in the plasma to decompose. The higher the proportion of those phases is, the faster the subsequent quenching was, freezing them in a non-equilibrium state.

Rf-SPS coatings seem to contain about 20 wt% of secondary phases. This value is too high according to the ISO 13779 - part 3 standard which stipulates that each crystalline phase other than hydroxyapatite should not represent > 5 wt% of the total crystalline phases. Calcium Oxide (CaO) is particularly critical since it causes serious damages to coatings when immersed into an aqueous medium because of its volume expansion to 50% resulting from its hydrolysis into $Ca(OH)_2$ [37]. All coatings are compliant in this sense, with however a higher proportion of CaO in rf-SPS coatings. The high crystallinity ratios 93% for K-SPS and 84% for Q-SPS coating, indicate a sufficient heat flux onto the coating during plasma spraying to promote an active annealing of the various deposited CaP phases. For both rf-SPS coatings the proportion of hydroxyapatite is quite the same but K-SPS comprises more TCP (8.5 ± 0.3% for K-SPS and 2.6 ± 0.2% for Q-SPS) while Q-SPS contains more TTCP (8.0 ± 0.4% for K-SPS and 15.3 ± 0.3% for Q-SPS).

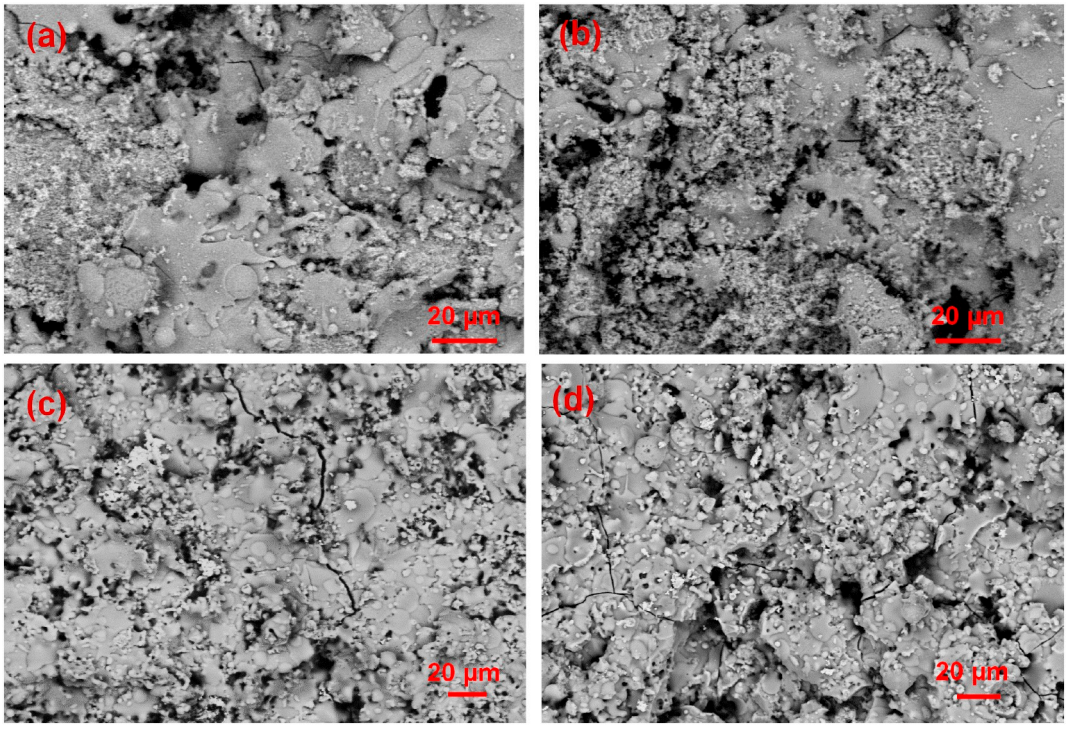

Fig. 3. Images of surfaces acquired by SEM: (a) Blocky-APS; (b) SD-APS; (c) K and (d) Q SPS-coatings.

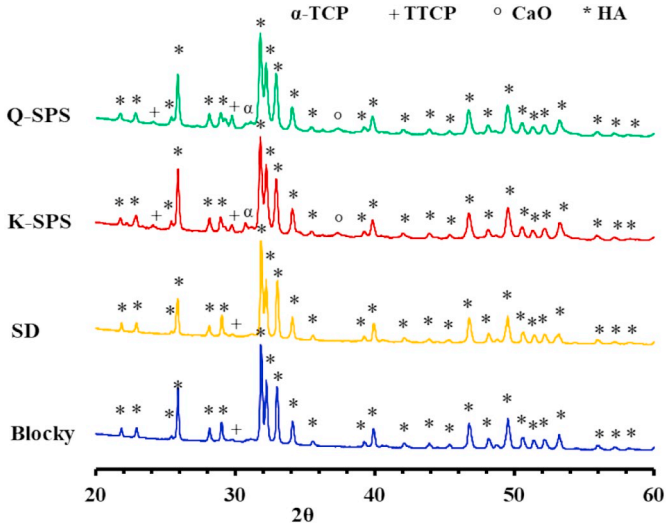

Fig. 4. XRD of coatings surfaces obtained by APS and SPS with assignments of the peaks to the phases.

Table V
Crystalline composition of APS and SPS coatings obtained with Rietveld refinement of XRD data.

Phases (%)	APS	APS	SPS	SPS
	Blocky	Spray-dried	K-SPS	Q-SPS
HA	91.4 ± 0.4	92.5 ± 0.7	81.3 ± 0.3	80.2 ± 0.3
β-TCP	1.1 ± 0.3	/	0.1 ± 0.2	0.1 ± 0.2
α-TCP	1.2 ± 0.3	1.2 ± 0.5	8.5 ± 0.3	2.6 ± 0.2
TTCP	5.9 ± 0.4	6.1 ± 0.6	8.0 ± 0.4	15.3 ± 0.3
CaO	0.3 ± 0.06	0.2 ± 0.2	1.4 ± 0.06	1.3 ± 0.04
ACP	4.10^{-2} ± 0.5	4.10^{-2} ± 0.9	0.7 ± 0.7	0.4 ± 0.5
Rw (%)	6.7	7.8	7.4	6.0
Rwnb (%)	16.6	18.8	15.8	12.8
Crystallinity ratio (%)	76	77	93	84

This could be on one hand the consequence of the Ca/P ratio of the respective powders, since the diagram of the quasi-binary CaO-P_2O_5-(H_2O) system stipulates that for a Ca/P ratio of 1.62 in equilibrium state at room temperature, K-SPS powder should be composed of a mixture of HA and TCP [44,45]. Nevertheless, some phosphorus is always evaporated during the process [9,12], which should bring the ratio of the related coating a little closer to 1.67. Q-SPS particles have a stoichiometric Ca/P ratio, which means that the decomposition follows the Eqs. (1a)-(5) and one could expect that the higher proportion of HA should give less secondary phases than K-SPS powder at the same spraying conditions. But on the other hand, even though they exhibit a stoichiometric Ca/P ratio, Q-SPS particles have smaller size than K-SPS particles, making them more sensitive to high temperatures due to their greater exchange surface. As they pass through the plasma, the decomposition of the apatite particles may thus be enhanced [46], explaining the similar HA proportion for both SPS coatings. Evaporation of phosphorus is also to be remembered, as it very likely brought the total Ca/P ratio of Q-SPS coatings over 1.67, favoring the formation of CaO and TTCP at high temperatures. Rietveld refinements reveal a low proportion of amorphous phase ACP in the XRD patterns of K-SPS and Q-SPS coatings in contrast to the amount of the other secondary phases. Since the CaP particles hit the substrate in a highly decomposed/amorphous state, this either mean that the surface temperature is sufficient (at least 600 °C [47]) to allow the partial or total recrystallisation of the amorphous phase into hydroxyapatite, or this could mean that the temperature is high enough (between 1350 °C and 1700 °C) to sustain or even increase the decomposition on the surface, resulting into a larger proportion of TTCP or TCP, while turning ACP into other crystalline phases. Since decomposition of HA happens between 1350 and 1570 °C [2], such a phenomenon can take place and has been already mentioned in other works [48]. Besides, even though the substrate is constantly cooled down, the plasma jet can be so elongated that a very high amount of heat can be transferred to the substrate/coating.

In contrast to the important transformation of the feedstocks in rf-SPS, APS coatings compositions are compliant with the values summoned in standards and were produced in such a way that their crystalline characteristics were identical. There is few ACP but some TTCP

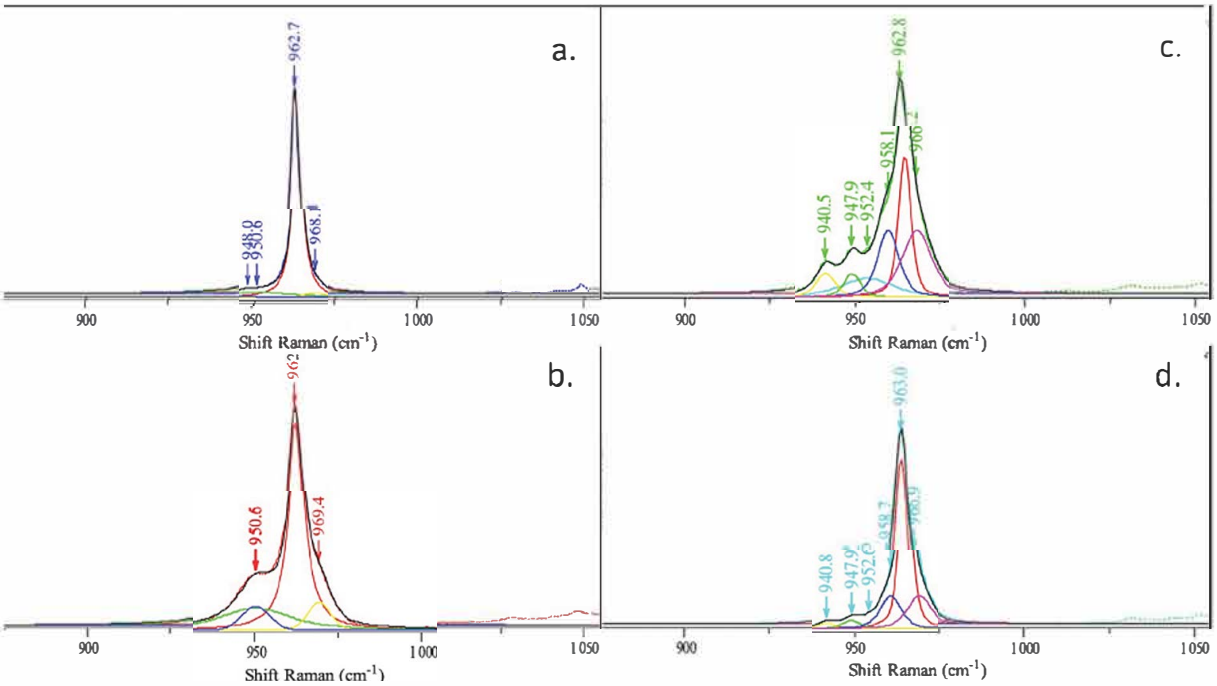

Fig. 5. Raman spectra of a. blocky-APS, b. SD-APS, c. Q-SPS and d. K-SPS coatings.

and TCP are present in very similar proportion, and CaO is almost completely absent. Those coatings present all the typical characteristics of plasma sprayed coatings with a good control and limitation of the decomposition process. Crystallinity ratios are noticeably the same (76% and 77% for blocky and SD-coatings respectively), but are lower than in rf-SPS coatings, which may have an incidence on their biological properties since many works highlighted the increased cell proliferation and adhesion with the crystallinity of the CaP coating [27], not to mention the improvement of in vivo stability.

Typical Raman spectra of all APS and rf-SPS coatings (Fig. 5) display complementary results from those obtained by XRD. Interestingly, when comparing APS coatings (Fig. 5a and b), more ACP and oxyapatite are detected in SD-coatings. This suggests that the thermal treatment of the SD powder inside the plasma jet was more advanced with a faster quenching than for the blocky powder, even though XRD patterns show similar crystalline patterns. TTCP phase is not detected, probably hidden by the overlapping of ACP and oxyapatite bands. Raman spectra of rf-SPS coatings (Fig. 5 c and d) show consistent results with XRD, with very distinct peaks attributed to the TTCP phase at 940 and 946 cm^{-1}. ACP and oxyapatite are not detected, or slightly present but in lower proportion than TTCP, which highlights the amorphous character of the APS coatings compared with SPS-coatings, accordingly to the crystallinity ratio but not to the Rietveld refinements values. XRD is not suited to evaluate the proportion of amorphous phase compared to Raman spectroscopy, thus the latter technique is preferred.

3.2.1.3. Superimposition of phases cartography and topography. Both K-SPS and Q-SPS Raman cartographies were superimposed with the topography of the same area obtained by optical profilometry, to see a possible correlation between the coating topography and its composition. The yellow/white spots on the Raman mapping indicate a high proportion of hydroxyapatite while the blue ones indicate a lower proportion. Although some areas contain more hydroxyapatite than others, no direct correlation with specific areas of the topography (either valleys, peaks or plateau) could be established by superimposing the Raman cartography of K-SPS coating with its profilometry map in Fig. 6. The areas containing a similar amount of hydroxyapatite cover from a few to about 50 μm^2. They could likely represent a splat and highlight the various thermal treatments undergone by the particles within the plasma. This analysis evidences the composition heterogeneity of hydroxyapatite plasma-sprayed coatings.

3.2.2. In coating morphology and microstructure

3.2.2.1. Thickness and porosity. Thickness was in the same range of values for both APS coatings, but blocky-coatings were slightly thicker than SD-coatings (137 µm ± 15 and 112 µm ± 20 respectively, Fig. 7c and d). This in consistent with the fact that blocky powder is denser than spray-dried powder: for the same spraying conditions, a fewer loss of material occurs due to a higher inertia. Overall, rf-SPS coatings made with K-SPS powder are 1.7 times thicker (around 80 µm, Fig. 7 a) than those made with Q-SPS powders (~45 µm, Fig. 7 b).

All the deposited coatings have total porosity values quite similar to those determined by image analysis. But SD-APS and Q-SPS coatings are slightly more porous (19.4 ± 3.1% and 19.3 ± 4.2% respectively) than Blocky-APS and K-SPS (15.8 ± 2.4% and 14.4 ± 3.0% respectively). These results must be considered carefully since they strongly depend on the image analysis protocol including cross-sections preparation. Nevertheless, it remains relevant to compare them, and it seems that for both plasma spray techniques, the thicker coating is also the denser.

3.2.2.2. In-thickness microstructure. Both rf-SPS coatings appear to be homogenously structured with splats of about 0.7 µm ± 0.2 thick (Table V, Fig. 7a and b), but K-SPS coating is denser and some semi-molten particles are visible in Q-SPS coating, conferring a granular bimodal structure [49]. Many hydroxyapatite plasma-sprayed coatings have already shown a granular structure [50], indicating that some particles are not fully molten during spraying. EDS analysis showed that grey areas present in the coating are composed of calcium phosphates. But since the signal of calcium, oxygen and phosphorus is weaker in these areas than in white ones, one can conclude that the density is lower, explaining this darker shade. The white/dense areas are made of crystalline hydroxyapatite and decomposition phases, while grey/porous areas are unmolten hydroxyapatite particles. The presence of those unmolten zones can be related to the precursor particle size and density. As mentioned before, small particles are less efficiently

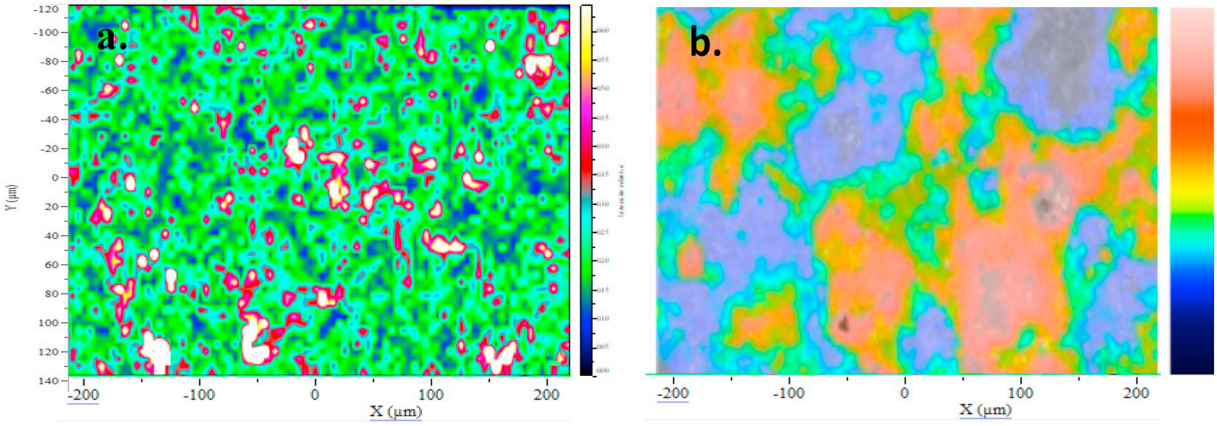

Fig. 6. a. Raman cartography of the R_2 ratio and b. topography of the same area of 440 × 265 µm^2, for K-SPS coating (valleys in blue, peaks in red).

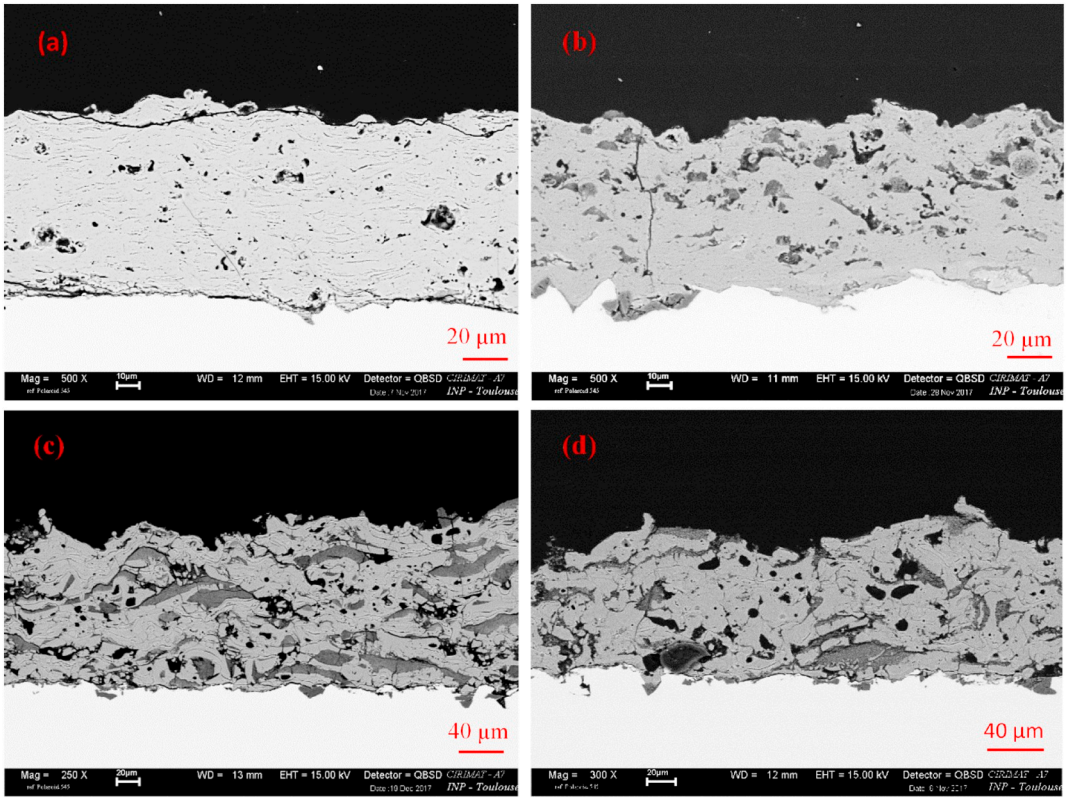

Fig. 7. Cross-section SEM images of (a) K, (b) Q SPS coatings and (c) Blocky, (d) Spray-dried APS coatings acquired by BSE imaging.

accelerated by the gas than large ones. Therefore their impact on the substrate is softer, and the particles tend to retrieve their granular structure due to high surface tension that takes over before the solidification occurs [21]. These granular zones have a diameter equal or below 6 µm in the case of Q-SPS coating. It represents 3 times less the volume of the initial atomized drop being around 17 µm, which not only confirms the fragmentation phenomenon but also shows that the use of Q-SPS suspension enables the formation of smaller CaP droplets than K-SPS suspension. The granular structure may also be due to the high reactivity of small particles to the thermophoresis force caused by the thermal gradient inside the plasma. They are ejected to the coldest temperatures and solidified before the impact on the surface. In contrast APS coatings (Fig. 7 c and d) display much larger microstructure features than rf-SPS coatings as expected. Both coatings contain fully and partially melted zone as well, which reflect the non-uniformity of the plasma thermal treatment of powders. Splats are from 2.2 to 19 µm and from 1.8 to 17 µm thick in the case of blocky and SD-APS coatings respectively. The Blocky-coating exhibits a few more unmolten parts, which could be attributed to the larger particle mean diameter and density.

The cross-section Raman cartography of the K-SPS coating (Fig. 8) displays a more distinct presence of HA nearby the top surface, decreasing as it gets closer to the substrate. This is in agreement with what is usually noticed in HA plasma sprayed coatings [2,12]. Indeed, as the molten material impacts the cooled substrate, it quenches and maintains the high temperature phases due to HA decomposition. As the calcium phosphate is deposited, the previously deposited layers form an insulating layer due to their characteristic low thermal conductivity. The calcium phosphate lamellae retain more thermal energy by being gradually more isolated from the cooled substrate and can thus recover their most stable structure that is hydroxyapatite. This could explain why K are better crystallized than Q-SPS coatings: their larger thickness

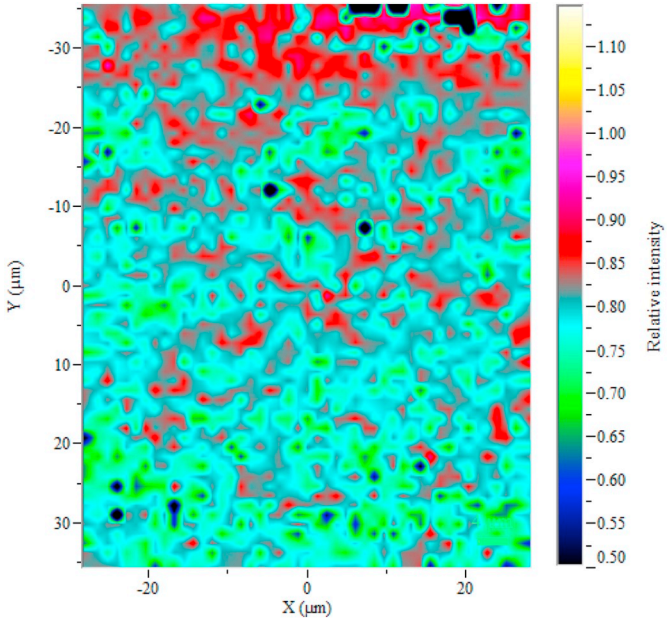

Fig. 8. Raman cartography of the R_2 ratio of the K-SPS coating's cross section.

constitutes a more efficient thermal barrier against the cooled substrate. Zhang et al. [48] showed that depending on the spraying distance, TCP and TTCP could appear on the substrate during the process. The substrate temperature thus needs to be adjusted and controlled in such a way that the particles are neither drastically quenched nor led to further decomposition. The presence of fractures on the surface and at the substrate-coating interface supports the 2nd hypothesis because it requires a very high thermal dilatation to reach this level of mechanical stress. The same trend has been commonly observed with Q-SPS coating, both APS coatings in this study and more generally in other works [4].

4. Conclusions

In the present study, two different precursors noted K-SPS and Q-SPS were synthesized to formulate suspensions to be implemented in rf-SPS. Although these particles have a similar crystallinity ratio around 70%, the former is deficient in calcium with a crystallite size of about 20 nm and a grain size centered at 9 µm while the latter is stoichiometric with a crystallite size of about 70 nm and a grain size centered at 3 µm. The results showed that the crystallinity ratios of rf-SPS coatings are as high as 93% in contrast to the 75% currently achieved for APS coatings. The Ca/P ratio of the precursors influenced the proportion of TTCP (from 8 to 15%) and TCP (from 2.6 to 8.5%) crystalline secondary phases which are in both rf-SPS coatings around 20% in total. In comparison, the amount of hydroxyapatite in APS coatings is around 90%. Therefore rf-SPS allows producing highly crystallized nanostructured coatings, disclosing the possible control of their biological behavior. The precursor size distribution was shown to be a decisive parameter for APS but not for rf-SPS coatings, whose microstructures were more influenced by the size of the atomized suspension drops. Finally, the heterogeneous distribution of the phases on the surface of rf-SPS coatings was demonstrated by Raman cartography, which could be of major interest for understanding the anchoring of proteins and cells onto the implant surface.

Acknowledgements

This work is supported by the Agence Nationale de la Recherche of France under project named ARCHICAP (ANR-15-CE19-0021) and the Région Occitanie in France under project named REVAMITIC (CLE).

References

[1] Registre canadien des remplacements articulaires (RCRA), Arthroplasties de la hanche et du genou au Canada, Rapport annuel de 2014–2015, 2015 http://ovidsp.ovid.com/ovidweb.cgi?T=JS&PAGE=reference&D=emed9&NEWS=N&AN=38724890.
[2] I. Demnati, D. Grossin, C. Combes, C. Rey, Plasma-sprayed apatite coatings: review of physical-chemical characteristics and their biological consequences, J. Med. Biol. Eng. 34 (2014) 1–7, https://doi.org/10.5405/jmbe.1459.
[3] R.A. Surmenev, A review of plasma-assisted methods for calcium phosphate-based coatings fabrication, Surf. Coat. Technol. 206 (2012) 2035–2056, https://doi.org/10.1016/j.surfcoat.2011.11.002.
[4] R.B. Heimann, Plasma-sprayed hydroxylapatite-based coatings: chemical, mechanical, microstructural, and biomedical properties, J. Therm. Spray Technol. 25 (2016) 827–850, https://doi.org/10.1007/s11666-016-0421-9.
[5] R.B. Heimann, Osseoconductive and corrosion-inhibiting plasma-sprayed calcium phosphate coatings for metallic medical implants, Metals (Basel, Switz.) 7 (2017) 1–19, https://doi.org/10.3390/met7110468.
[6] FDA, Guidance for Industry and FDA Staff Non-clinical Information for Femoral Stem Prostheses, 16 (2007) http://www.fda.gov/medicaldevices/deviceregulationandguidance/guidancedocuments/ucm071275.htm.
[7] M.R. Mucalo, Hydroxyapatite (HAp) for Biomedical Applications, (2015), https://doi.org/10.1016/C2013-0-16440-9.
[8] Y.C. Tsui, C. Doyle, T.W. Clyne, Plasma sprayed hydroxyapatite coatings on titanium substrates. Part 2: optimisation of coating properties, Biomaterials 19 (1998) 2031–2043, https://doi.org/10.1016/S0142-9612(98)00104-5.
[9] K.A. Gross, C.C. Berndt, Thermal processing of hydroxyapatite for coating production, J. Biomed. Mater. Res. 39 (1998) 580–587.
[10] S. Overgaard, Calcium phosphate coatings for fixation of bone implants: evaluated mechanically and histologically by stereological methods, Acta Orthop. Scand. 71 (2000) 1–74, https://doi.org/10.1080/000164700753595574.
[11] D.E. Macdonald, F. Betts, M. Stranick, S. Doty, A.L. Boskey, Physicochemical study of plasma-sprayed hydroxyapatite-coated implants in humans, J. Biomed. Mater. Res. 54 (2001) 480–490.
[12] R.B. Heimann, Tracking the thermal decomposition of plasma-sprayed hydroxylapatite, Am. Mineral. 100 (2015) 2419–2425.
[13] S.R. Radin, P. Ducheyne, The effect of calcium phosphate ceramic composition and structure on in vitro behavior. I. Dissolution, J. Biomed. Mater. Res. 27 (1993) 25–34, https://doi.org/10.1002/jbm.820270106.
[14] S.R. Radin, P. Ducheyne, Plasma spraying induced changes of calcium phosphate ceramic characteristics and the effect on in vitro stability, J. Mater. Sci. Mater. Med. 3 (1992) 33–42, https://doi.org/10.1007/BF00702942.
[15] T.J. Webster, C. Ergun, R.H. Doremus, R.W. Siegel, R. Bizios, Enhanced functions of osteoblasts on nanophase ceramics, Biomaterials 21 (2000) 1803–1810.
[16] M. Roy, A. Bandyopadhyay, S. Bose, Induction plasma sprayed nano hydroxyapatite coatings on titanium for orthopaedic and dental implants, Surf. Coat. Technol. 205 (2011) 2785–2792, https://doi.org/10.1016/j.surfcoat.2010.10.042.
[17] E. Bouyer, F. Gitzhofer, M.I. Boulos, Suspension plasma spraying for hydroxyapatite powder preparation by RF plasma, IEEE Trans. Plasma Sci. 25 (1997) 1066–1072, https://doi.org/10.1109/27.649627.
[18] P.L. Fauchais, J.V.R. Heberlein, M.I. Boulos, Thermal Spray Fundamentals, Springer, Kindle, 2014, https://doi.org/10.1007/978-0-387-68991-3.
[19] L. Pawlowski, Suspension and solution thermal spray coatings, Surf. Coat. Technol. 203 (2009) 2807–2829, https://doi.org/10.1016/j.surfcoat.2009.03.005.
[20] H. Li, K.A. Khor, P. Cheang, Effect of steam treatment during plasma spraying on the microstructure of hydroxyapatite splats and coatings, Proc. Int. Therm. Spray Conf. 15 (2006) 610–616, https://doi.org/10.1361/105996306X146938.
[21] P. Fauchais, Suspension and solution plasma spraying, J. Phys. D. Appl. Phys. 46 (2013), https://doi.org/10.1088/0022-3727/46/22/224015 14 pp..
[22] N. Atsuchi, T. Watanabe, Numerical Modeling of Non-equilibrium Argon-Oxygen Induction Plasmas under Atmospheric Pressure, Asian Pacific Confed. Chem. Eng., 2004, pp. 1–10.
[23] K. Wang, C. Zhou, Y. Hong, X. Zhang, A Review of Protein Adsorption on Bioceramics, 2 Interface Focus, 2012, pp. 259–277, https://doi.org/10.1098/rsfs.2012.0012.
[24] R.B. Heimann, Structure, properties, and biomedical performance of osteoconductive bioceramic coatings, Surf. Coat. Technol. 233 (2013) 27–38, https://doi.org/10.1016/j.surfcoat.2012.11.013.
[25] N. Aebli, J. Krebs, H. Stich, P. Schawalder, M. Walton, D. Schwenke, H. Gruner, B. Gasser, J.C. Theis, In vivo comparison of the osseointegration of vacuum plasma sprayed titanium- and hydroxyapatite-coated implants, J. Biomed. Mater. Res., Part A 66 (2003) 356–363, https://doi.org/10.1002/jbm.a.10508.
[26] D. Buser, R.K. Schenk, S. Steinemann, J.P. Fiorellini, C.H. Fox, Influence of surface characteristics on bone integration of titanium implants: a histomorphometric study in miniature pigs, J. Biomed. Mater. Res. 25 (1991) 889–902.
[27] R.A. Surmenev, M.A. Surmeneva, A.A. Ivanova, Significance of calcium phosphate coatings for the enhancement of new bone osteogenesis - a review, Acta Biomater. 10 (2014) 557–579, https://doi.org/10.1016/j.actbio.2013.10.036.
[28] P. Ducheyne, Comprehensive Materials, Elsevier Science, 2011.
[29] S. Kannan, J.M.F. Ferreira, Synthesis and thermal stability of hydroxyapatite-β-tricalcium phosphate composites with cosubstituted sodium, magnesium, and fluorine, Chem. Mater. 18 (2006) 198–203, https://doi.org/10.1021/cm051966i.
[30] N.S. Al-Qasas, S. Rohani, Synthesis of pure hydroxyapatite and the effect of synthesis conditions on its yield, crystallinity, morphology and mean particle size, Sep. Sci. Technol. 40 (2005) 3187–3224, https://doi.org/10.1080/

01496390500385400.
[31] International standard ISO_13779, Implants for Surgery – Hydroxyapatite – Part 3: Chemical Analysis and Characterization of Crystallinity and Phase Purity, (2008).
[32] Internation standard ISO_13779, Implants for Surgery – Hydroxyapatite – Part 2: Coatings of Hydroxyapatite, (2008).
[33] J. Zhao, J. Zhao, J. Chen, X. Wang, Z. Han, Y. Li, Rietveld refinement of hydroxyapatite, tricalcium phosphate and biphasic materials prepared by solution combustion method, Ceram. Int. 40 (2014) 3379–3388, https://doi.org/10.1016/j.ceramint.2013.09.094.
[34] L. Keller, W.A. Dollase, X-ray determination of crystalline hydroxyapatite to amorphous calcium- phosphate ratio in plasma sprayed coatings, J. Biomed. Mater. Res. 49 (2000) 244–249, https://doi.org/10.1002/(SICI)1097-4636(200002)49:2<244::AID-JBM13>3.0.CO;2-H.
[35] C. Rey, O. Marsan, C. Combes, C. Drouet, D. Grossin, S. Sarda, Characterization of calcium phosphates using vibrational spectroscopies, Adv. Calcium Phosphate Biomater. (2014), https://doi.org/10.1007/978-3-319-02904-7.
[36] K. Geels, D.B. Fowler, W.-U. Kopp, M. Rückert, Material/Preparation Tables—Methods C-01/T-01 to C-68/T-68, Metallogr. Mater. Specim. Prep. Light Microsc. Image Anal. Hardness Test., 2006, pp. 223–226 https://books.google.cl/books?id=oaehZy3Vo1kC.
[37] I. Demnati, M. Parco, D. Grossin, I. Fagoaga, C. Drouet, G. Barykin, C. Combes, I. Braceras, S. Goncalves, C. Rey, Hydroxyapatite coating on titanium by a low energy plasma spraying mini-gun, Surf. Coat. Technol. 206 (2012) 2346–2353, https://doi.org/10.1016/j.surfcoat.2011.10.025.
[38] P.S. Prevéy, X-ray diffraction characterization of crystallinity and phase composition in plasma-sprayed hydroxyapatite coatings, J. Therm. Spray Technol. 9 (2000) 369–376, https://doi.org/10.1361/105996300770349827.
[39] L. Berzina-Cimdina, N. Borodajenko, Research of Calcium Phosphates Using Fourier Transform Infrared Spectroscopy, Infrared Spectrosc. – Mater. Sci. Eng. Technol., 2012, pp. 123–148, https://doi.org/10.5772/36942.
[40] S. Koutsopoulos, Synthesis and Characterization of Hydroxyapatite Crystals: a Review Study on the Analytical Methods, Wiley Period. Inc., 2002, pp. 31–34, https://doi.org/10.1002/jbm.10280.
[41] S. Raynaud, E. Champion, D. Bernache-Assollant, P. Thomas, Calcium phosphate apatites with variable Ca/P atomic ratio I. Synthesis, characterisation and thermal stability of powders, Biomaterials 23 (2002) 1065–1072, https://doi.org/10.1016/S0142-9612(01)00218-6.
[42] Y.C. Tsui, C. Doyle, T.W. Clyne, Plasma sprayed hydroxyapatite coatings on titanium substrates. Part 1: mechanical properties and residual stress levels, Biomaterials 19 (1998) 2015–2029, https://doi.org/10.1016/S0142-9612(98)00103-3.
[43] P. Fauchais, M. Vardelle, J.F. Coudert, A. Vardelle, C. Delbos, J. Fazilleau, Thermal plasma deposition from thick to thin coatings and from micro- to nanostructure, Pure Appl. Chem. 77 (2005) 475–485, https://doi.org/10.1351/pac200577020475.
[44] S. Ramesh, C. Tan, M. Hamdi, I. Sopyan, W. Teng, The Influence of Ca/P Ratio on the Properties of Hydroxyapatite Bioceramics, 6423 Proc. SPIE - Int. Soc. Opt. Eng., 2007, https://doi.org/10.1117/12.779890.
[45] M.T. Carayon, J.L. Lacout, Study of the Ca/P atomic ratio of the amorphous phase in plasma-sprayed hydroxyapatite coatings, J. Solid State Chem. 172 (2003) 339–350, https://doi.org/10.1016/S0022-4596(02)00085-3.
[46] R. Kumar, P. Cheang, K.A. Khor, RF plasma processing of ultra-fine hydroxyaptite powders, J. Mater. Process. Technol. 113 (2001) 456–462, https://doi.org/10.1016/S0924-0136(01)00611-2.
[47] R. Kumar, P. Cheang, K.A. Khor, Phase composition and heat of crystallisation of amorphous calcium phosphate in ultra-fine radio frequency suspension plasma sprayed hydroxyapatite powders, Acta Mater. 52 (2004) 1171–1181, https://doi.org/10.1016/j.actamat.2003.11.016.
[48] C. Zhang, H. Xu, X. Geng, J. Wang, J. Xiao, P. Zhu, Effect of spray distance on microstructure and Tribological performance of suspension plasma-sprayed hydroxyapatite – titania composite coatings, J. Therm. Spray Technol. 25 (2016) 1255–1263, https://doi.org/10.1007/s11666-016-0453-1.
[49] P. Fauchais, G. Montavon, G. Bertrand, From powders to thermally sprayed coatings, J. Therm. Spray Technol. 19 (2010) 56–80, https://doi.org/10.1007/s11666-009-9435-x.
[50] R.T. Candidato, P. Sokołowski, L. Łatka, S. Kozerski, L. Palowski, A. Denoirjean, Plasma spraying of hydroxyapatite coatings using powder, suspension and solution feedstocks, Weld. Technol. Rev. 87 (2015) 64–71.